

Computational Thermal Analysis of Divergent and Convergent Flow Channels for Cooling Plates in PEM Fuel Cells

Mahmut Caner ACAR^{1*}

¹ Nigde Omer Halisdemir University, Engineering Faculty, Mechanical Engineering Department, Nigde, Türkiye

(ORCID:0000-0002-6206-5374)



Keywords: CFD, Fluid flow, Heat transfer, Cooling, PEM fuel cell.

Abstract

During the operation of polymer electrolyte membrane fuel cells excess heat is generated as a result of electrochemical reactions. This heat raises the temperature of the polymer electrolyte membrane fuel cells, which can damage the membrane. Homogeneity of the temperature through the fuel cell is important in terms of stability and performance. Thermal management is therefore essential and is provided by the cooling channels formed on the bipolar plates or cooling plates. In this paper, a three-dimensional computational analysis of the cooling plate with divergent and convergent flow field designs is carried out. In this context, heat transfer and fluid flow performances of these two different flow fields are considered in terms of temperature uniformity, maximum temperature and pressure drop. Numerical results demonstrated that the more uniform temperature distribution along the fuel cell could be achieved with divergent flow field design. Furthermore, when a divergent design is used, the maximum surface temperature of the cooling plate and the pressure drop between the inlet and outlet of the channel are reduced.

1. Introduction

Due to the depletion of fossil fuels caused by its over consumption and increased dependence on energy, studies have been focused on new energy sources. In addition, the use of conventional fossil fuels as energy sources causes environmental pollution and climate changes. For those reasons, attentions on new energy sources have been increased. Hydrogen is seen as one of most popular environmentally friendly energy sources, especially when used in fuel cell applications. Among the fuel cell types, the PEM fuel cells have superior advantages such as higher power density, lower operating temperature, silent operation and rapid start up [1], [2]. Thus, these fuel cells can be preferred in many fields such as automobile industries, military applications and stationary power systems [3].

The schematic of a PEM fuel cell components and its cooling channel are shown in Figure 1. The hydrogen and air/oxygen enter the cell from anode

and cathode sides, respectively. While the hydrogen oxidation reactions take place in anode side, Equation (1), oxygen reduction reactions take place in the cathode side, Equation (2). Only water and heat are produced as by product during these electrochemical reactions, Equation (3).

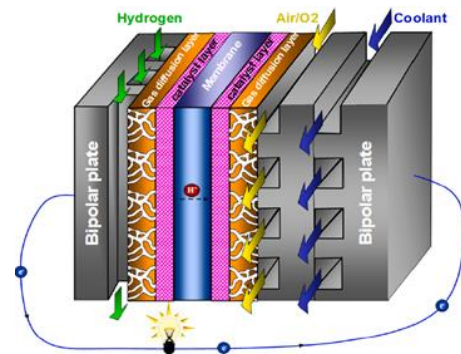
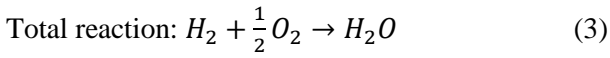
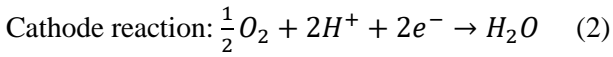
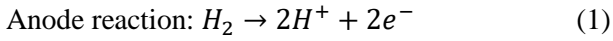


Figure 1. PEM fuel cell components and cooling channel [4].

*Corresponding author: mahmutcaneracar@ohu.edu.tr

Received: 18.12.2022, Accepted: 03.03.2023



In addition to water, heat is also generated as a result of electrochemical reactions. This excess heat causes the cell temperature to rise excessively over time and damages the membrane. Therefore, it needs to be removed from the cell by a proper cooling method. Usually, the cooling plates are made of either graphite or metallic materials. The most commonly used metallic materials are stainless steel, aluminum, titanium and its alloys [5]–[8]. The flow channels are machined when graphite is used as cooling plate. However, in addition to machining, stamping, hydroforming or roll forming methods are also utilized in the case of metallic plates [9]–[12]. The cooling fluids are circulated through the flow fields formed on cooling plates. There are many types of flow field designs considered in the literature [2], [13]–[15]. The most practical designs are serpentine, parallel and parallel-serpentine [16]. Using different flow field designs has some advantages and disadvantages. For example, some of them are superior in terms of heat removal performance, however, they may lead to higher pressure drops, resulting in higher pumping power [17], [18]. Thus, both the thermal and hydraulic performances of the cooling plates should be evaluated together.

Many flow channel types, including both conventional parallel, serpentine, parallel-serpentine and some other special designs, have been studied by researchers in the literature [19]–[23]. The effects of different flow field designs on thermal performance for a graphite cooling plate with an area of $18 \times 18 \text{ cm}^2$ were computationally investigated by Baek et al. [17]. In this context, two conventional serpentine designs (Model A and Model B), two multi pass serpentine designs (Model C and Model D), one parallel design (Model E) and one spiral design (Model F) were considered. According to their results, the Model C and Model D showed better thermal performance than the Model A and Model B. The Model E exhibited the smallest pressure drop, while the worst temperature distribution was obtained with this design. Ravishankar et al. [24] performed a detailed numerical analysis on flow field types for one conventional serpentine and one conventional spiral design and four novel designs, including distributed serpentine, divided serpentine, distributed spiral and divided spiral. The cooling plate was made of aluminum. The highest and lowest pressure drop

values were obtained with divided spiral (many turn regions) and conventional serpentine designs, respectively. The distributed serpentine design presented the best temperature uniformity with 25% progress over the serpentine type. Rahgoshay et al. [25] simulated a PEM fuel cell with two traditional serpentine parallel flow field designs. They also compared the results obtained from the cooling plates with an isothermal model (constant temperature). The results showed that the value of maximum temperature was almost the same for serpentine and parallel design. However, about 24% improvement was observed in temperature uniformity when serpentine design was considered as flow field. They also indicated that the cooling flow fields should be considered during the numerical analysis of a PEM fuel cell to obtain more accurate temperature distribution inside the fuel cell. In another study, Ghasemi et al. [26] conducted a simulation study for a PEM fuel cell with conventional serpentine type reactant flow field. The simulations were carried out for six different cooling channel designs: one traditional parallel, one traditional serpentine, one traditional spiral, and three different novel designs. Even if a largest pressure drop was obtained with traditional spiral flow field design, the lowest temperature difference of 3.38 K and lowest temperature uniformity index (U_T) of 0.58 K were also achieved with this channel type.

According to the open literature, there are many studies on flow field design of cooling plates in PEM fuel cells. Mostly, spiral, serpentine, parallel and parallel-serpentine flow fields were evaluated in those researches. In this paper, unconventional divergent and convergent flow field designs are investigated. For this purpose, a cooling plate made of graphite with a $10 \times 10 \text{ cm}^2$ area is used in the computational fluid dynamic (CFD) analysis. The CFD studies were carried out with Ansys-Fluent commercial program. The heat removal and fluid flow performances of divergent and convergent flow fields were compared in terms of temperature uniformity, maximum temperature and fluid pressure drop.

2. Material and Method

In order to build a fuel cell stack and produce the required output power, many fuel cell units are typically serially connected. A coolant circulates through the channels of cooling plates and absorbs the heat produced to prevent the fuel cell from overheating. Figure 2a shows the geometry of cooling plates with the divergent and convergent flow fields used in this study. The cooling plate thickness

is 2 mm and it has 32 flow channels for both designs. The dimension of the channel is seen in Figure 2b. The channel width increases and decreases with an angle of 0.57 degrees from inlet to outlet for divergent and convergent flow fields, respectively. The divergent flow field design has an inlet width of 1 mm

and an outlet width of 2 mm. In the case of convergent design, the inlet width is 2 mm, and the outlet width is 1 mm. The channel deep for both flow fields is 1 mm.

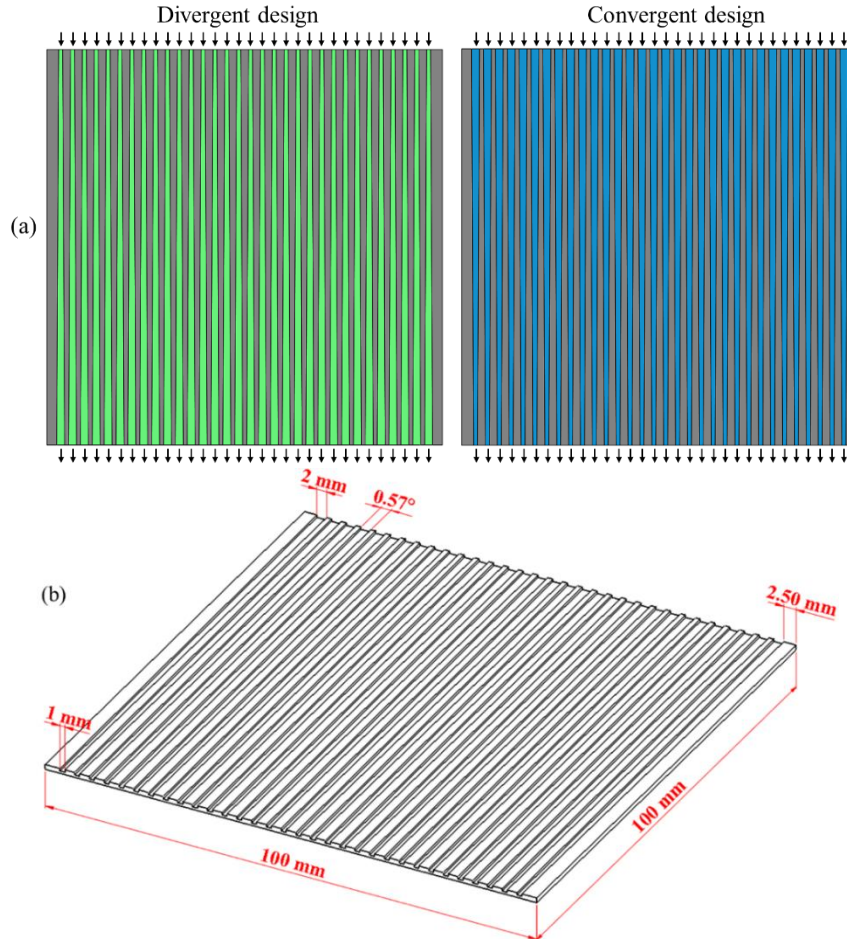


Figure 2. (a) Divergent and convergent flow fields, (b) dimension of the channel.

2.2. Governing equations

A comprehensive simulation of fluid flow and heat transfer within the cooling plates was performed using the commercial CFD program Ansys-Fluent. The finite volume discretization technique is used in this software to solve the mass conservation, momentum and energy equations. The governing equations for the Newtonian, laminar, steady state and incompressible fluid flow across the cooling plate are as follows:

$$\frac{\partial u_j}{\partial x_j} = 0 \quad (4)$$

$$\rho \left(\mathbf{u}_j \frac{\partial u_i}{\partial x_j} \right) = \frac{\partial p}{\partial x_i} + \frac{\partial}{\partial x_j} \left(\mu \frac{\partial u_i}{\partial x_j} \right) \quad (5)$$

$$\rho c_p \left(\mathbf{u}_j \frac{\partial T}{\partial x_j} \right) = \frac{\partial}{\partial x_j} \left(\mathbf{k} \frac{\partial T}{\partial x_j} \right) \quad (6)$$

where \mathbf{u} is the velocity, p is the pressure and T is the temperature. In addition, \mathbf{k} , ρ , c_p and μ are the thermal conductivity, density, specific heat capacity and dynamic viscosity, respectively.

The energy equation for the solid regions is described with Equation (7).

$$\frac{\partial}{\partial x_j} \left(\mathbf{k} \frac{\partial T}{\partial x_j} \right) = 0 \quad (7)$$

2.3. Operating and boundary conditions

In the simulation process, water is selected as coolant and graphite is used as cooling plate

material. Table 1 shows the thermo-physical properties of graphite. Since the thermo-physical properties of water vary with temperature, the polynomial functions represented by Eqs. (8)-(10) were applied to the program [27]. However, because the change in C_p at the temperatures considered was so small (less than 1%), this property was kept constant during the simulations at 4179 J/kg K. The coolant enters the channel at a constant temperature of 40 °C. Four different mass flow rates (\dot{m}) of 8.0×10^{-4} kg/s, 1.6×10^{-3} kg/s, 2.4×10^{-3} kg/s and 3.2×10^{-3} kg/s are considered during the numerical analysis. The value used for the surface heat flux (q'') is 5000 W/m² which is typical for PEMFCs under normal operating conditions [17]. Also, Equation (11) can be used to determine the generated heat flux for each cell during the PEM fuel cell operation. The operating parameters for the simulation are seen in Table 1.

$$\mu = 0.258 \times 10^{-10}T^4 - 0.358 \times 10^{-7}T^3 + 0.186 \times 10^{-4}T^2 - 0.432 \times 10^{-2}T + 0.378 \quad (8)$$

$$k = 0.754 \times 10^{-9}T^4 - 0.988 \times 10^{-6}T^3 + 0.474 \times 10^{-3}T^2 - 0.974 \times 10^{-1}T + 7.745 \quad (9)$$

$$\rho = -0.180 \times 10^{-6}T^4 + 0.248 \times 10^{-3}T^3 - 0.131T^2 + 30.824T - 1690.497 \quad (10)$$

$$Q_i = (1.23 - V_i)i \quad (11)$$

where 1.23 is the value of open circuit voltage, V_i is the working voltage of the PEM fuel cell and i is the electrical current density.

Table 1. Thermo-physical properties of graphite and operating conditions.

Parameters	Values	Units
Cooling plate properties		
Density	2250	kg/m ³
Specific heat capacity	690	J/kg K
Thermal conductivity	24	W/m K
Operating conditions		
Coolant inlet temperature	40	°C
Coolant mass flow rate	8.0×10^{-4} , 1.6×10^{-3} , 2.4×10^{-3} , 3.2×10^{-3}	kg/s
Heat flux	5000	W/m ²

Figure 3 depicts the cooling plate's half domain together with symmetry boundary condition, heat flux boundary condition, solid and coolant regions. The heat flux is implemented on the bottom surface of the cooling plate. To reduce the computational time, cooling plate's half domain is considered and therefore, symmetrical boundary condition is applied in the CFD analysis. A constant mass flow rate boundary condition and a constant pressure condition are applied at the channel inlets and outlets, respectively.

2.4. Numerical procedure and model validation

A 3D finite volume technique is used to numerically solve the governing equations within the computational domain. The pressure and velocity fields are linked using the well-known Coupled

algorithm. The least squares cell-based gradient is considered for the spatial discretization. The second order upwind scheme is used for the momentum and energy equations, whereas the second order method is chosen for pressure. The computations are considered to have converged when the residuals of the continuity, momentum and energy equations fall below 1×10^{-4} , 1×10^{-7} and 1×10^{-9} , respectively.

To prove the accuracy of the numerical results, a grid dependence analysis is also conducted. For this purpose, the outputs of five different grid structures with element numbers of 364,958, 839,020, 1,453,500, 1,986,264 and 2,545,272 are compared with each other. The grid dependence test of the divergent and convergent flow fields based on the coolant outlet temperature is shown in Figure 4a. As can be seen from the

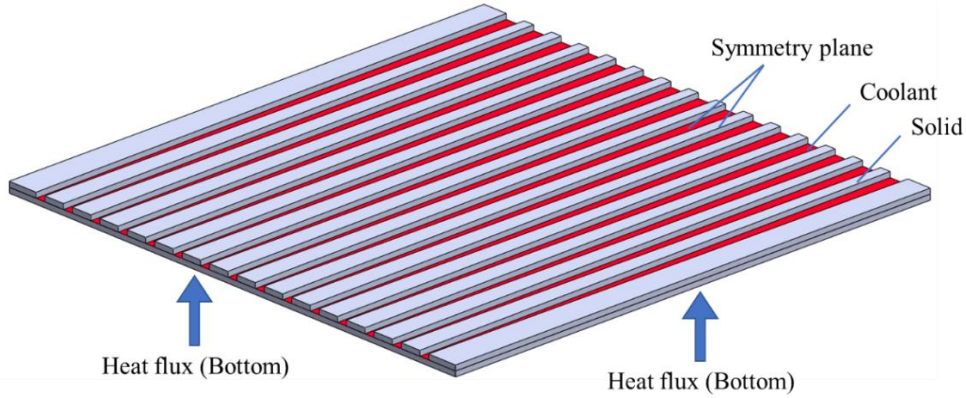


Figure 3. Boundary conditions for the cooling plate half domain.

figure, the variation in outlet temperature is very small after element number of 1,986,264 for both divergent and convergent channels. Similarly, a small change is obtained in pressure drop between the inlet and outlet of the channel when the element number exceeds the same value (Figure 4b). Therefore, a grid structure with 1,986,264 elements is chosen in the simulation analysis.

To verify the numerical results obtained from the CFD analysis, an experimental study done by Raghuraman et al. was considered [28]. For this

purpose, simulation results obtained for the coolant temperature at the channel outlet and pressure drop between the inlet and outlet of the channel were compared with the experiment as depicted in Figure 5. Figure 5a shows that the simulation results and experimental data agree well for whole Reynolds number values ranging from 50 to 350, with a maximum deviation of 5.3%. Figure 5b displays that the values of pressure drop computed numerically for the complete Reynolds number are quite close to those measured experimentally.

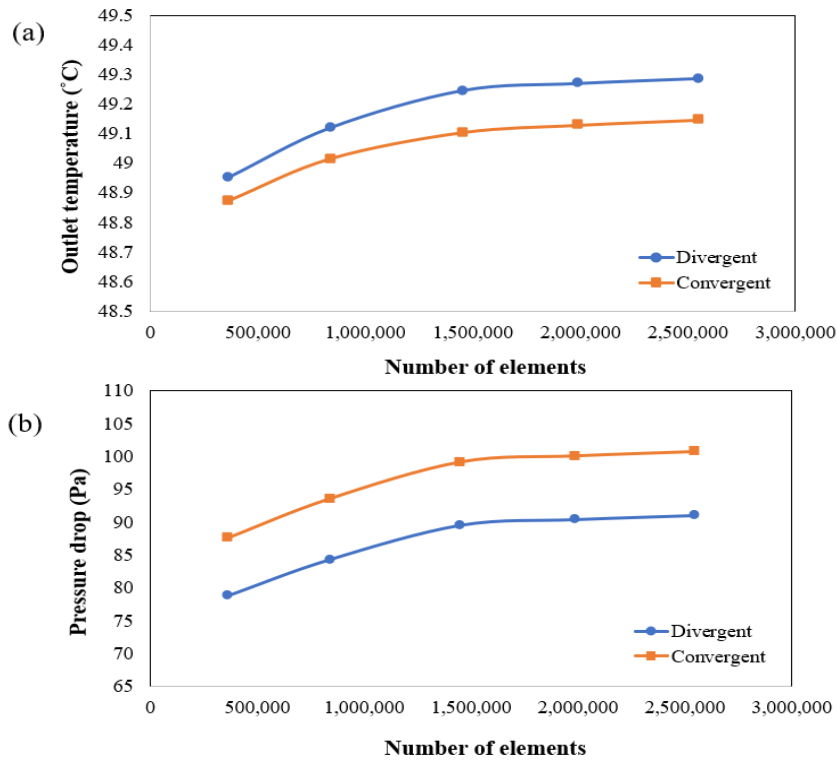


Figure 4. Grid dependence test for (a) coolant outlet temperature, (b) pressure drop.

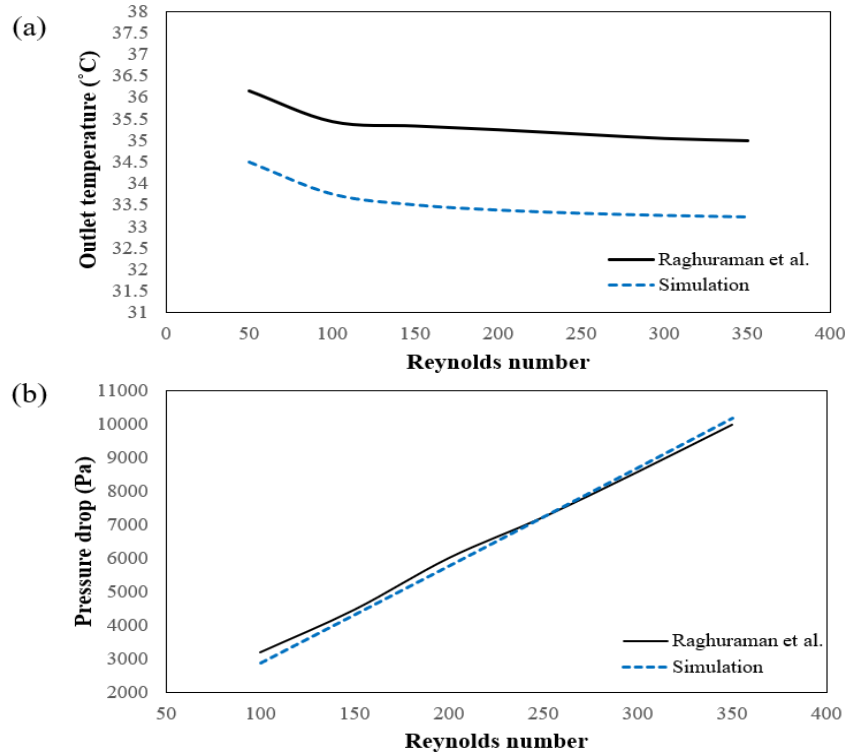


Figure 5. Model validation study for (a) outlet temperature, (b) pressure drop.

3. Results and Discussion

For various mass flow rates of 8.0×10^{-4} kg/s, 1.6×10^{-3} kg/s, 2.4×10^{-3} kg/s and 3.2×10^{-3} kg/s, the thermal and fluid flow performances of the cooling plate with divergent and convergent flow fields are investigated in terms of temperature uniformity, maximum temperature and pressure drop. Throughout the simulation, the coolant inlet temperature and heat flux imposed from the bottom surface of the cooling plate are kept constant at 40 °C and 5000 W/m², respectively.

It is critical for the stability and performance of the PEM fuel cells to maintain as uniform a temperature as possible. There is a criterion known as the index of uniform temperature (IUT) [29] for analyzing the temperature homogeneity at a surface area. The IUT has been utilized in thermal applications where temperature distribution is essential. The difference between the surface temperature and the average surface temperature at the heat transfer surface can be measured quantitatively using the IUT. In other words, IUT equals zero when the temperature distribution is entirely uniform. The IUT is calculated by the following equation:

$$IUT = \frac{\int_A |T - T_{avg}| dA}{\int_A dA} \quad \text{and} \quad T_{avg} = \frac{\int_A T dA}{\int_A dA} \quad (12)$$

where T is the surface temperature, T_{avg} is the average surface temperature and A is the surface area. Equation (12) is only applicable on the heat flux boundary conditions [30].

Table 2 shows the simulation results of maximum and minimum surface temperatures (T_{max} and T_{min}), temperature difference (ΔT) between T_{max} and T_{min} , IUT and pressure drop (ΔP) at an inlet temperature (T_{in}) of 40 °C, a heat flux of 5000 W/m² and a mass flow rate of 1.6×10^{-3} kg/s. T_{max} and ΔT are lower in the divergent channels by 0.35 °C and 0.63 °C, respectively. In addition, smaller IUT is obtained for divergent flow fields, which can be considered as an improvement in temperature distribution along the heat flux surface. As a result, using a divergent channel instead of a convergent one improves temperature uniformity by 11.77%. The divergent channel also reduces the pressure drop by 7.93%, indicating that less pumping power is required. The % Improvement is determined by Equation (13) as follows:

Table 2. Simulation results for divergent and convergent flow fields.

Parameters	Divergent channel	Convergent channel	% Improvement
T_{\max} (°C)	53.89	54.24	-
T_{\min} (°C)	41.54	41.27	-
ΔT (°C)	12.34	12.97	-
IUT (°C)	2.02	2.29	11.79
ΔP (Pa)	83.01	90.17	7.94

$$\%Improvement = \frac{|x_c - x_d|}{x_c} \times 100 \quad (13)$$

where x_c and x_d are the calculated values obtained from convergent and divergent flow field designs, respectively.

For convergent and divergent flow fields, the distribution of temperature at the bottom surface of cooling plate is seen in Figure 6. Here, mass flow rate, coolant inlet temperature and heat flux are 1.6×10^{-3} kg/s, 40 °C and 5000 W/m², respectively. The coolant temperature rises from the inlet to the outlet of the channels due to the continuous

absorption of reaction heat by the coolant. Highest surface temperature of 54.3 °C and 53.9 °C are obtained in case of convergent and divergent flow fields, respectively. Furthermore, when a convergent channel is used, higher temperature zones are observed at the end corner regions. Figure 7 represents the change in temperature distribution at the cooling plate's symmetry plane under the same operating conditions as in Figure 6. Similarly, while temperatures are lower near the inlet region, they are higher closer to the channel outlet. In the case of convergent channel design, the highest temperature is obtained.

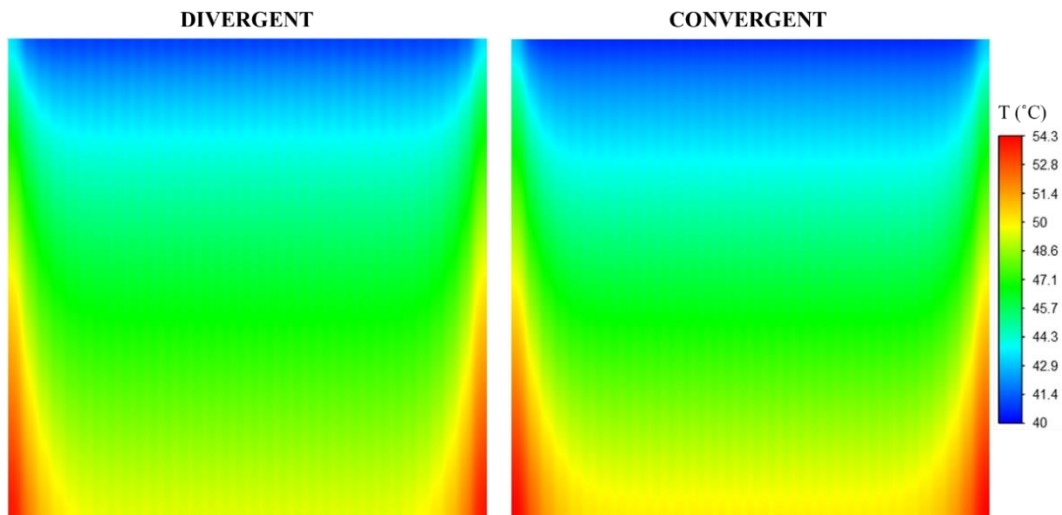
**Figure 6.** Distribution of temperature at the bottom surface.

Figure 8 depicts the pressure drop distribution between the inlet and outlet of the cooling channels with an inlet coolant temperature of 40 °C, a mass flow rate of 1.6×10^{-3} kg/s, and a heat flux of 5000 W/m². As illustrated in the figure, the pressure drops along the coolant channels are greater in the convergent design, indicating higher pumping power.

Figure 9 shows the changes in IUT as a function of coolant mass flow rate at a constant

inlet temperature and heat flux. Because increasing mass flow rate causes a decrease in cooling plate surface temperature, the IUT declines with coolant flow rate. Lower IUT values are observed for divergent flow design at all coolant flow rates. At high mass flow rates, the %Improvement takes greater values. Since the lowest IUTs are obtained in the case of divergent channels, it can be said that a more uniform temperature distribution can be achieved with this design.

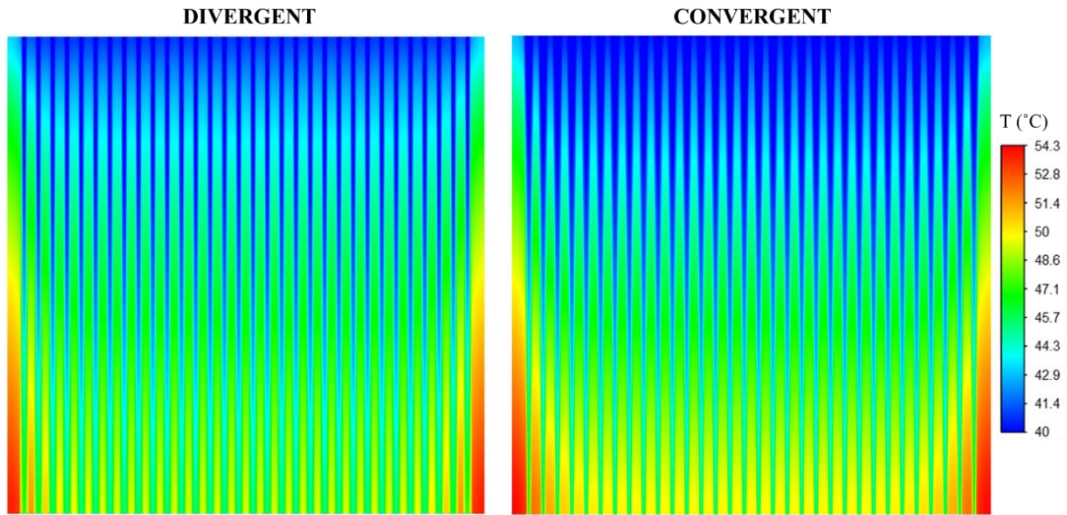


Figure 7. Distribution of temperature at the symmetry surface.

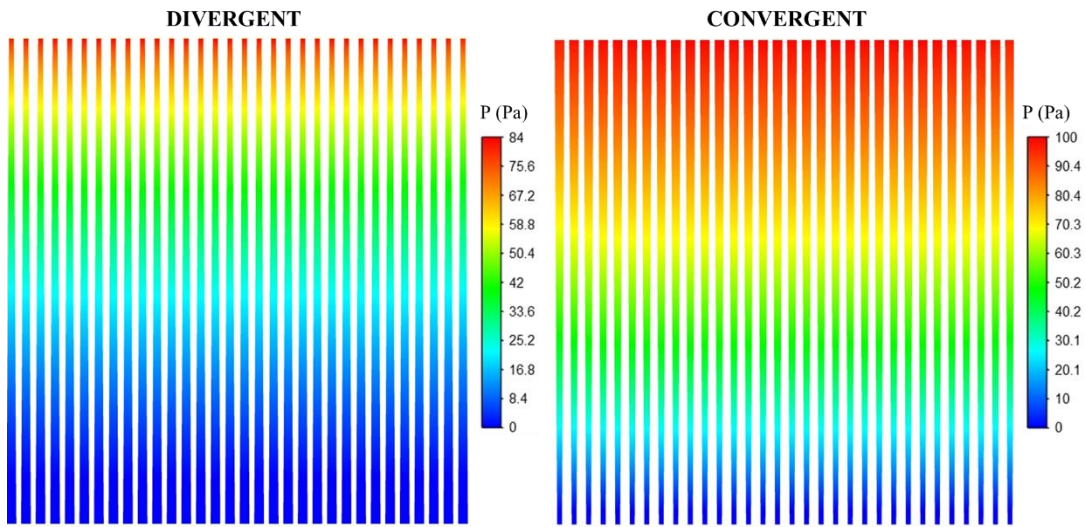


Figure 8. Distribution of pressure drop along the cooling channels.

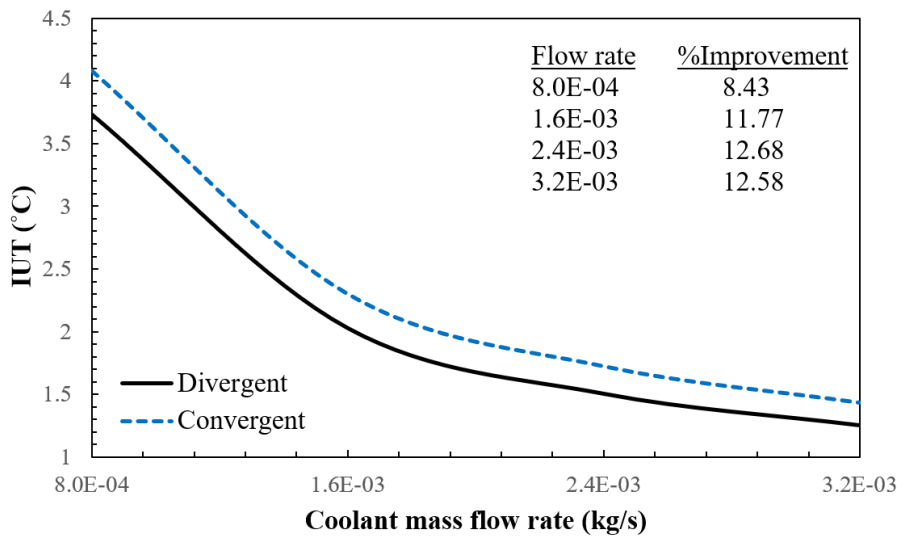


Figure 9. Variation of IUT with mass flow rate ($T_{in} = 40 \text{ }^\circ\text{C}$, $q'' = 5000 \text{ W/m}^2$).

Figure 10 displays the variation in average temperature at the cooling plate's bottom surface for two channel designs. The average surface temperature decreases as the coolant mass flow rate increases. At low flow rates, the difference in average surface temperature between divergent and convergent channels is quite small; however, it gets greater values at higher mass flow rates.

Maintaining the cooling plate's maximum surface temperature at a specific level is crucial for ensuring the thermal stability of the cell. In fact, it is the most crucial factor in avoiding thermal damage. The maximum temperature of two channel designs along the cooling plate bottom surface is presented in Figure 11. As expected, the mass flow rate has a negative effect on the maximum surface

temperature, and it can cause a decrease in this parameter for both channel designs. The maximum surface temperature difference between divergent and convergent channels decreases very slowly with mass flow rate. It is $0.33\text{ }^{\circ}\text{C}$ at the mass flow rate of $8.0 \times 10^{-4}\text{ kg/s}$ and $0.23\text{ }^{\circ}\text{C}$ at the mass flow rate of $3.2 \times 10^{-3}\text{ kg/s}$.

The temperature difference results between maximum and minimum bottom surface temperature are plotted in Figure 12. Again, based on the coolant mass flow rate, a decreasing trend in temperature difference can be seen. According to the graph, the divergent design has lower temperature differences at whole mass flow rate ranges, which may result in an improvement in IUT.

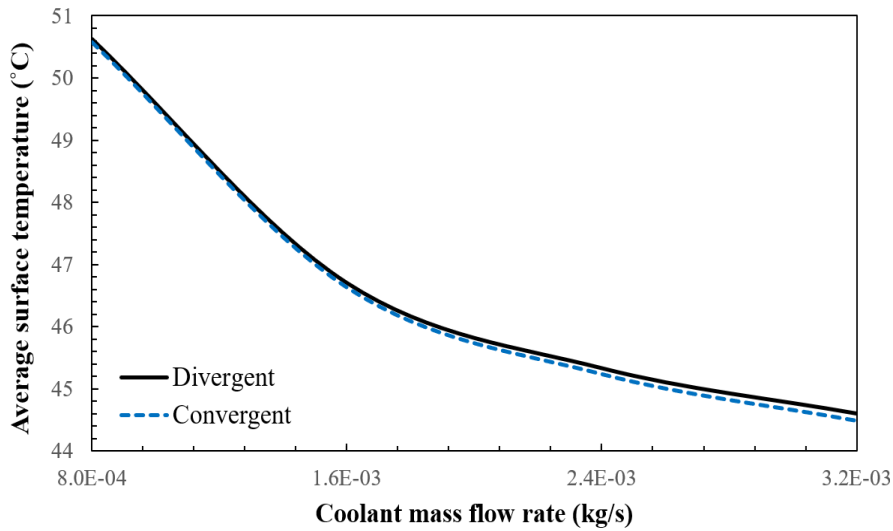


Figure 10. Variation of average temperature with mass flow rate ($T_{in} = 40\text{ }^{\circ}\text{C}$, $q'' = 5000\text{ W/m}^2$).

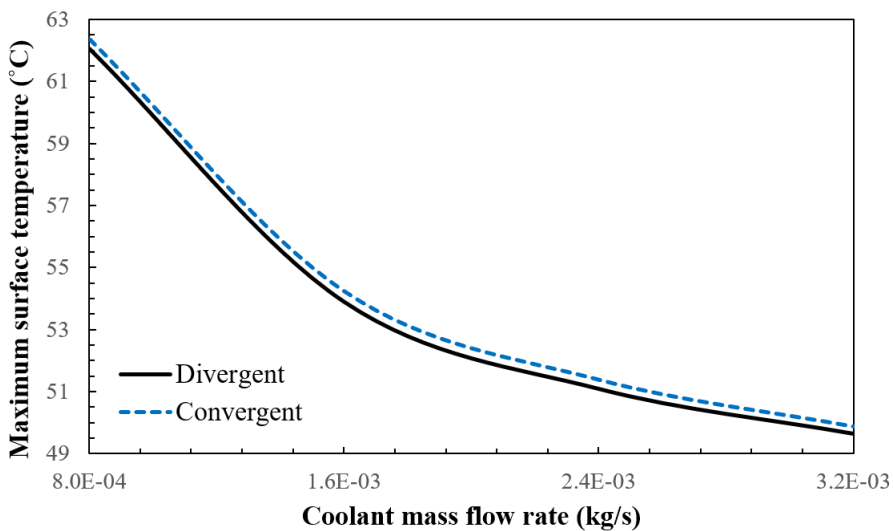


Figure 11. Variation of maximum temperature with mass flow rate ($T_{in} = 40\text{ }^{\circ}\text{C}$, $q'' = 5000\text{ W/m}^2$).

Figure 13 depicts the simulated influence of coolant mass flow rate on pressure drop for two different designs. As it is seen in the figure, lower pressure drop values are obtained with divergent flow field, indicating low pumping power requirements. This is due to the higher velocity values of the coolant in the divergent channel. It is clearly shown in Figure 13 that the difference

between two designs is small at low flow rates and becomes larger as the mass flow rate increases. When using a divergent flow field design instead of a convergent one, pressure drop would be reduced by 1.00%, 7.93%, 12.89%, and 17.04% at mass flow rates of 8.0×10^{-4} kg/s, 1.6×10^{-3} kg/s, 2.4×10^{-3} kg/s, and 3.2×10^{-3} kg/s, respectively.

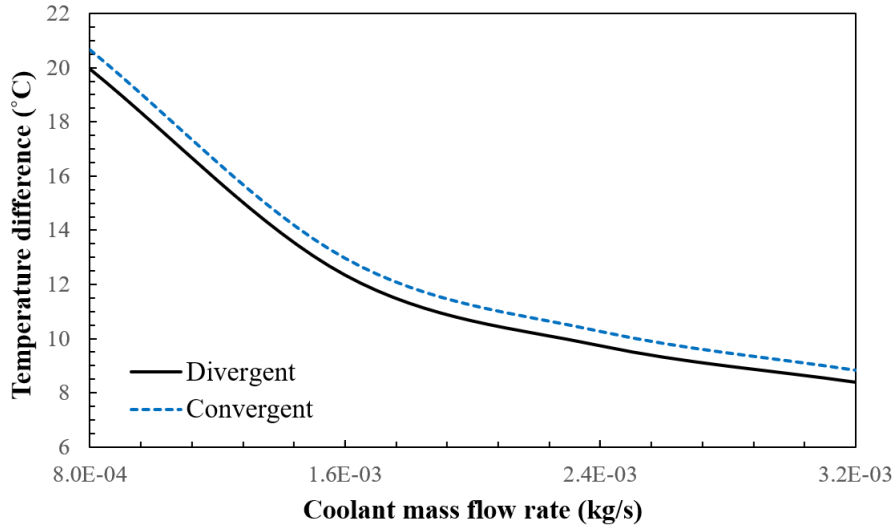


Figure 12. Variation of temperature difference with mass flow rate ($T_{in} = 40 \text{ }^\circ\text{C}$, $q'' = 5000 \text{ W/m}^2$).

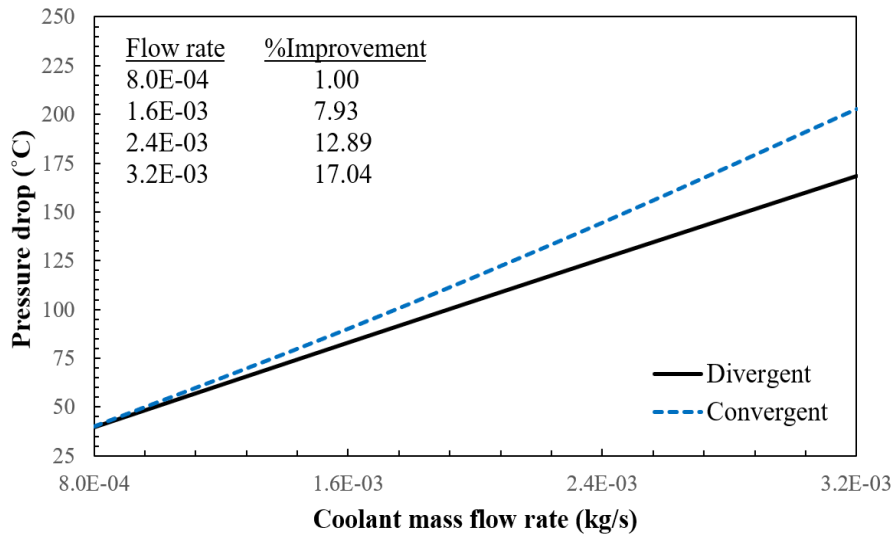


Figure 13. Variation of pressure drop with mass flow rate ($T_{in} = 40 \text{ }^\circ\text{C}$, $q'' = 5000 \text{ W/m}^2$).

4. Conclusion and Suggestions

A numerical study was conducted for a graphite cooling plate with a $10 \times 10 \text{ cm}^2$ area. In this context, the heat transfer and fluid flow performances of divergent and convergent flow field designs were investigated and compared. The cooling performance of these two designs were simulated according to the

temperature uniformity, maximum temperature on bottom surface and pressure drop between inlet and outlet of the flow channels. While the coolant inlet temperature ($40 \text{ }^\circ\text{C}$) and heat flux (5000 W/m^2) were kept constant during the simulation, the coolant flow rates were varied from 8.0×10^{-4} kg/s to 3.2×10^{-3} kg/s.

Increasing coolant mass flow rates reduced IUT, maximum surface temperature, average surface

temperature and temperature difference between maximum and minimum surface temperatures. The pressure drop, on the other hand, increased as the flow rate increased. The uniformity of the temperature through the bottom surface of the cooling plate improved by 8.43%, 11.77%, 12.68% and 12.58% at the mass flow rates of 8.0×10^{-4} , 1.6×10^{-3} , 2.4×10^{-3} and 3.2×10^{-3} , respectively, when divergent design was considered instead of convergent design. Therefore, it can be concluded that the divergent flow field design provides a more uniform temperature across the cooling plate. Divergent design also resulted in lower maximum temperature values on the bottom surface of the cooling plate. In the case of divergent flow channel, the pressure drop was reduced by up to 17.04%.

In conclusion, it was discovered that the divergent flow field design was the more efficient design for sustaining more uniform temperature distribution across the cooling plate or fuel cell active area. In addition, because divergent channel design produced lower pressure drops, this design would require less pumping power. Overall, the findings of this paper will be useful for designing PEM fuel cell cooling systems as well as other applications where thermal management and fluid flow are important.

Statement of Research and Publication Ethics

The study is complied with research and publication ethics.

References

- [1] E. Afshari and S. A. Jazayeri, "Effects of the cell thermal behavior and water phase change on a proton exchange membrane fuel cell performance," *Energy Convers. Manag.*, vol. 51, no. 4, pp. 655–662, 2010, doi: 10.1016/j.enconman.2009.11.004.
- [2] S. A. Atyabi and E. Afshari, "A numerical multiphase CFD simulation for PEMFC with parallel sinusoidal flow fields," *J. Therm. Anal. Calorim.*, vol. 135, no. 3, pp. 1823–1833, 2019, doi: 10.1007/s10973-018-7270-3.
- [3] Y. Wang, K. S. Chen, J. Mishler, S. C. Cho, and X. C. Adroher, "A review of polymer electrolyte membrane fuel cells: Technology, applications, and needs on fundamental research," *Appl. Energy*, vol. 88, no. 4, pp. 981–1007, 2011, doi: 10.1016/j.apenergy.2010.09.030.
- [4] Y. Wang, "Modeling of two-phase transport in the diffusion media of polymer electrolyte fuel cells," *J. Power Sources*, vol. 185, no. 1, pp. 261–271, 2008, doi: 10.1016/j.jpowsour.2008.07.007.
- [5] H. Pourrahmani *et al.*, "A Review on the Long-Term Performance of Proton Exchange Membrane Fuel Cells: From Degradation Modeling to the Effects of Bipolar Plates, Sealings, and Contaminants," *Energies*, vol. 15, no. 14, 2022, doi: 10.3390/en15145081.
- [6] Y. Song *et al.*, "Review on current research of materials, fabrication and application for bipolar plate in proton exchange membrane fuel cell," *Int. J. Hydrogen Energy*, vol. 45, no. 54, pp. 29832–29847, 2020, doi: 10.1016/j.ijhydene.2019.07.231.
- [7] R. A. Antunes, M. C. L. Oliveira, G. Ett, and V. Ett, "Corrosion of metal bipolar plates for PEM fuel cells: A review," *Int. J. Hydrogen Energy*, vol. 35, no. 8, pp. 3632–3647, 2010, doi: 10.1016/j.ijhydene.2010.01.059.
- [8] K. Xiong, W. Wu, S. Wang, and L. Zhang, "Modeling, design, materials and fabrication of bipolar plates for proton exchange membrane fuel cell: A review," *Appl. Energy*, vol. 301, no. June, 2021, doi: 10.1016/j.apenergy.2021.117443.
- [9] Y. Leng, P. Ming, D. Yang, and C. Zhang, "Stainless steel bipolar plates for proton exchange membrane fuel cells: Materials, flow channel design and forming processes," *J. Power Sources*, vol. 451, no. October 2019, p. 227783, 2020, doi: 10.1016/j.jpowsour.2020.227783.
- [10] S. Porstmann, T. Wannemacher, and W. G. Drossel, "A comprehensive comparison of state-of-the-art manufacturing methods for fuel cell bipolar plates including anticipated future industry trends," *J. Manuf. Process.*, vol. 60, no. October, pp. 366–383, 2020, doi: 10.1016/j.jmapro.2020.10.041.
- [11] M. M. Barzegari and F. A. Khatir, "Study of thickness distribution and dimensional accuracy of stamped metallic bipolar plates," *Int. J. Hydrogen Energy*, vol. 44, no. 59, pp. 31360–31371, 2019, doi: 10.1016/j.ijhydene.2019.09.225.
- [12] H. Talebi-Ghadikolaee, M. Elyasi, and M. J. Mirnia, "Investigation of failure during rubber pad forming of metallic bipolar plates," *Thin-Walled Struct.*, vol. 150, no. February, p. 106671, 2020, doi: 10.1016/j.tws.2020.106671.
- [13] E. Alizadeh, S. M. Rahgoshay, M. Rahimi-Esbo, M. Khorshidian, and S. H. M. Saadat, "A novel cooling

- flow field design for polymer electrolyte membrane fuel cell stack,” *Int. J. Hydrogen Energy*, vol. 41, no. 20, pp. 8525–8532, 2016, doi: 10.1016/j.ijhydene.2016.03.187.
- [14] X. Chen *et al.*, “Numerical study of a MIMO-shaped cooling plate in PEMFC stack for heat transfer enhancement,” *Energy Reports*, vol. 7, pp. 5804–5814, 2021, doi: 10.1016/j.egy.2021.09.010.
- [15] M. Saeedan, M. Ziaei-Rad, and E. Afshari, “Numerical thermal analysis of nanofluid flow through the cooling channels of a polymer electrolyte membrane fuel cell filled with metal foam,” *Int. J. Energy Res.*, vol. 44, no. 7, pp. 5730–5748, 2020, doi: 10.1002/er.5332.
- [16] S. Asghari, H. Akhgar, and B. F. Imani, “Design of thermal management subsystem for a 5 kW polymer electrolyte membrane fuel cell system,” *J. Power Sources*, vol. 196, no. 6, pp. 3141–3148, 2011, doi: 10.1016/j.jpowsour.2010.11.077.
- [17] S. M. Baek, S. H. Yu, J. H. Nam, and C. J. Kim, “A numerical study on uniform cooling of large-scale PEMFCs with different coolant flow field designs,” *Appl. Therm. Eng.*, vol. 31, no. 8–9, pp. 1427–1434, 2011, doi: 10.1016/j.applthermaleng.2011.01.009.
- [18] S. A. Atyabi, E. Afshari, E. Zohravi, and C. M. Udemu, “Three-dimensional simulation of different flow fields of proton exchange membrane fuel cell using a multi-phase coupled model with cooling channel,” *Energy*, vol. 234, p. 121247, 2021, doi: 10.1016/j.energy.2021.121247.
- [19] S. Li and B. Sundén, “Numerical study on thermal performance of non-uniform flow channel designs for cooling plates of PEM fuel cells,” *Numer. Heat Transf. Part A Appl.*, vol. 74, no. 1, pp. 917–930, 2018, doi: 10.1080/10407782.2018.1486642.
- [20] M. Seyhan, Y. E. Akansu, M. Murat, Y. Korkmaz, and S. O. Akansu, “Performance prediction of PEM fuel cell with wavy serpentine flow channel by using artificial neural network,” *Int. J. Hydrogen Energy*, vol. 42, no. 40, pp. 25619–25629, 2017, doi: 10.1016/j.ijhydene.2017.04.001.
- [21] B. Timurkutluk and M. Z. Chowdhury, “Numerical Investigation of Convergent and Divergent Parallel Flow Fields for PEMFCs,” *Fuel Cells*, vol. 18, no. 4, pp. 441–448, 2018, doi: 10.1002/fuce.201800029.
- [22] M. Z. Chowdhury and B. Timurkutluk, “Transport phenomena of convergent and divergent serpentine flow fields for PEMFC,” *Energy*, vol. 161, pp. 104–117, 2018, doi: 10.1016/j.energy.2018.07.143.
- [23] S. A. Ghadhban, W. H. Alawee, and H. A. Dhahad, “Study effects of bio-inspired flow filed design on Polymer Electrolyte Membrane fuel cell performance,” *Case Stud. Therm. Eng.*, vol. 24, no. May 2020, p. 100841, 2021, doi: 10.1016/j.csite.2021.100841.
- [24] S. Ravishankar and K. Arul Prakash, “Numerical studies on thermal performance of novel cooling plate designs in polymer electrolyte membrane fuel cell stacks,” *Appl. Therm. Eng.*, vol. 66, no. 1–2, pp. 239–251, 2014, doi: 10.1016/j.applthermaleng.2014.01.068.
- [25] S. M. Rahgoshay, A. A. Ranjbar, A. Ramiar, and E. Alizadeh, “Thermal investigation of a PEM fuel cell with cooling flow field,” *Energy*, vol. 134, pp. 61–73, 2017, doi: 10.1016/j.energy.2017.05.151.
- [26] M. Ghasemi, A. Ramiar, A. A. Ranjbar, and S. M. Rahgoshay, “A numerical study on thermal analysis and cooling flow fields effect on PEMFC performance,” *Int. J. Hydrogen Energy*, vol. 42, no. 38, pp. 24319–24337, 2017, doi: 10.1016/j.ijhydene.2017.08.036.
- [27] M. C. Acar, “Channel to rib width ratio effect on thermal performance of cooling plate in polymer electrolyte membrane fuel cell,” *Fuel Cells*, vol. 22, no. 5, pp. 154–168, 2022, doi: 10.1002/fuce.202200082.
- [28] D. R. S. Raghuraman, R. Thundil Karuppa Raj, P. K. Nagarajan, and B. V. A. Rao, “Influence of aspect ratio on the thermal performance of rectangular shaped micro channel heat sink using CFD code,” *Alexandria Eng. J.*, vol. 56, no. 1, pp. 43–54, 2017, doi: 10.1016/j.aej.2016.08.033.
- [29] F. C. Chen, Z. Gao, R. O. Loutfy, and M. Hecht, “Analysis of Optimal Heat Transfer in a PEM Fuel Cell Cooling Plate,” *Fuel Cells*, vol. 3, no. 4, pp. 181–188, 2003, doi: 10.1002/fuce.200330112.
- [30] E. Afshari, M. Ziaei-Rad, and M. M. Dehkordi, “Numerical investigation on a novel zigzag-shaped flow channel design for cooling plates of PEM fuel cells,” *J. Energy Inst.*, vol. 90, no. 5, pp. 752–763, 2017, doi: 10.1016/j.joei.2016.07.002.